Nanofloating gate modulated synaptic organic light-emitting transistors for reconfigurable displays

Yusheng Chen, Hanlin Wang, Feng Luo, Verónica Montes García, Zhaoyang Liu, Paolo Samorì

MATERIALS SCIENCE

Nanofloating gate modulated synaptic organic light-emitting transistors for reconfigurable displays

Yusheng Chen, Hanlin Wang, Feng Luo, Verónica Montes-García, Zhaoyang Liu, Paolo Samorì*

The use of postsynaptic current to drive long-lasting luminescence holds a disruptive potential for harnessing the next-generation of smart displays. Multiresponsive long afterglow emission can be achieved by integrating light-emitting polymers in electric spiked transistors trigged by distinct presynaptic signals inputs. Here, we report a highly effective electric spiked long afterglow organic light-emitting transistor (LAOLET), whose operation relies on a nanofloating gate architecture. Long afterglow emission with reconfigurable brightness and retention time is observed upon applying specific positive gate voltage spiked. Conversely, when negative gate voltage stimulus is applied, these LAOLETs function as click-on display. Interestingly, upon endowing the device with force sensing capabilities, it can operate as a long afterglow pressure sensor that emits long-lasting green light subsequently to a controlled extrusion action.

INTRODUCTION

Organic light-emitting transistors (OLETs) are unique platforms for optoelectronic applications. Their dual functionality, combining in a single device the light generation characteristic of light-emitting diodes with the current modulation and signal amplification of field-effect transistors, renders them particularly appealing for the development of the next generation of active matrix displays (*1*–*4*). Optically responsive memory OLETs, based on photochromic molecules or metal oxide with persistent photoconduction characteristics, have demonstrated significant potential for smart display technologies (*5*, *6*). However, these memory OLETs exhibit a major limitation: The memory current driving the light emission could be modulated solely by the optical stimulus. Hence, these devices do not fulfill the technological requirements for smart displays, which should be endowed with responsiveness to distinct bionic stimuli. To broaden the control over the device operation, thereby enabling functional diversification, electric spiked memory transistors could offer a versatile solution when coupled with sensors by collecting external physical or chemical stimuli and converting them into electrical inputs for data storage. The sensory data for intelligent bionic system could be thus encoded by using different types of stimuli, whose precision and reliability for technological applications have been already demonstrated through the fabrication of tactile sensors (*7*–*10*), light sensors (*11*–*13*), humidity sensors (*14*, *15*), and chemical sensors (*16*–*18*). As an alternative to conventional three-terminal memory architectures, nanofloating gate (NFG) transistors (NFGTs) are particularly suitable for the realization of both volatile and nonvolatile memory devices, because they combine a well-established working mechanism, reliable memory operations, and a gigantic memory capacity (*19*–*22*). Recently, artificial synaptic devices based on NFGTs have been exploited to mimic synaptic learning rules in human brain including short-term potentiation (STP)–to–long-term potentiation (LTP) transition and spike timing–dependent plasticity (STDP), empowering the development of neuromorphic computing hardware (*23*, *24*).

On the other hand, materials and processing optimization in organic optoelectronics enabled the controlled manufacturing of homogeneous large-area thin films deposited with cost-efficient and scalable liquid-based processing technologies such as spray and blade coating as well as ink jet and three-dimensional printing (*25*–*30*). Nevertheless, the stepwise assembly of superimposed multiple layers by mastering solution processing protocols requires the use of orthogonal solvents for the deposition of successive layers (*31*, *32*). While alcohol-soluble *n*-type polymers have been integrated as an electron transport layer in solution-processed hybrid OLETs (*33*, *34*), the use of alcohol-soluble hole transport/extraction polymers in high-performance organic optoelectronics still needs to be fully demonstrated (*35*, *36*), hitherto limiting their application in solution-processed *p*-type hybrid multilayer OLET architectures (*37*–*39*).

Here, we report full-color, NFG-modulated long afterglow OLETs (LAOLETs) whose "soft components" are all deposited by spin coating. The layout comprises superimposed layers of water-dispersed gold nanoparticles (Au NPs) as floating gate and methyl glycol–processed Al_2O_3 thin film as tunneling barrier, covered sequentially by a channel layer, a hole transport layer, a light-emitting layer (EML), and an electron transport layer, which are deposited from solutions in hot dichlorobenzene, chlorobenzene, toluene, and methanol, respectively. Interestingly, after applying positive gate spike as presynaptic stimulus, long afterglow electroluminescence with synaptic function of STP-to-LTP transition and STDP was observed. Conversely, upon applying a negative gate spike as signal input, immediate sparked electroluminescence was recorded. The time-dependent characterization revealed that two different targeted operating modes of retardation display and real-time display can be achieved in a single device. Hence, reconfigurable displays can be realized by the selecting polarity of gate voltage. Last, we demonstrated that, upon integrating a piezo-responsive sensor with these electrical spiked LAOLETs, long afterglow emission can be trigged by exerting an external pressure, suggesting their relevance for long afterglow sensing technologies.

RESULTS

An unprecedented class of all-solution-processed LAOLETs was developed by superimposing six functional layers. The device layout, supported on Si/SiO_2, comprises stacked layers of Au NPs/Al_2O_3/poly((2,3,5,6-tetrahydro-2,5-bis(2-octyldodecyl)-3,6-dioxopyrrolo(3,4-c)pyrrole-1,4-diyl)-2,5-thiophenediylthieno(3,2-b)thiophene-2,5-diyl-2,5

University of Strasbourg, CNRS, ISIS UMR 7006, 8 allée Gaspard Monge, F-67000 Strasbourg, France.
*Corresponding author. Email: samori@unistra.fr

thiophenediyl) (DPPDTT)/Au/poly(4-butylphenyl-diphenyl-amine) (PTPD)/EMLs/poly(9,9-bis(6-(*N*,*N*-diethylamino) hexyl)-fluorene-alt-9,9-bis(3-ethyl(oxetane-3-ethyoxy)-hexyl)-fluorene) (PFNOX)/Au, as portrayed in Fig. 1 (A and B). The emission of different colors (green, red, yellow, and blue) was obtained by using four commercial semiconducting light-emitting polymers, i.e., the green light-emitting spiro-copolymer (SpiroG), the red poly(2-methoxy-5-(3′,7′-dimethyloctyloxy)-1,4-phenylenevinylene) (MDMO-PPV), the yellow poly(9,9-dioctylfluorene-alt-bithiophene) (F8T2), and the blue poly(9,9-dioctylfluorene-co-bis-*N*,*N*-(4-butylphenyl)-bis-*N*,*N*-phenyl-1,4-phenylenediamine) (PFB). The chemical structure of the polymers is reported in Fig. 1D.

Fabrication and characteristics of NFG

First, floating gate synaptic transistors comprising a DPPDTT channel layer as active material were fabricated by using a bottom-gate, top-contact geometry to investigate the synaptic behavior (Fig. 2A). A stabilized suspension of 5-nm-sized Au NPs in citrate buffer solution was spin-coated onto a Si/SiO_2 wafer to act as NFG. Successively, an Al_2O_3 tunneling layer with a thickness of ~10 nm was spun from the Al_2O_3 precursor solution. The atomic force microscopy (AFM) images in Fig. 2 (B and C) confirms the relatively uniform microscale morphology of the Au NPs film after Al_2O_3 deposition. The space confinement of the Au NPs in between the two dielectric layers (SiO_2 and Al_2O_3 based) is expected to provide presynaptic weight tuning. The gate-source voltage (V_G) and the drain-source voltage (V_D) of NFGTs can be conceived as the pre- and postsynaptic terminals, respectively. The transfer curves of NFGTs under a variety of different ranges of V_G scanning conditions are displayed in Fig. 2D. As marked by the arrows, the V_G sweeping direction started from positive to negative (backward sweep direction) and then reversed to positive (forward sweep direction), resulting in a counterclockwise hysteresis. The NFGTs exhibited a predominant *p*-type behavior with a hole mobility of ca. 0.5 $cm^2 V^{-1} s^{-1}$. Typically, two distinct states were observed at two sweeping directions when the applied sweeping voltage exceeds ±40 V, revealing a negatively shifted threshold voltage (V_{Th}) in the backward sweep. Upon gradual expansion of the sweep range, the memory window of the devices, defined as the shifted V_{Th} (ΔV_{Th}), increased significantly. Maximum ΔV_{Th} with a value of 45 V was obtained after applying ±100 V to the gate. The transfer curves of NFGTs without Au NPs are plotted in fig. S1 for comparison, which present a lower ΔV_{Th} with a value of 20 V. This ΔV_{Th} can be exploited for writing/erasing operations in functional devices, whose working mechanism is displayed in Fig. 2 (E and F). When a suitable positive gate bias (>40 V) was applied to the gate terminal, electrons accumulated at the interface between the tunneling (Al_2O_3) layer and the channel layer, and some among them tunneled through the Al_2O_3 layer to be injected into Au NPs. These electrons were stored even after the removal of V_G because of the barrier provided by the Al_2O_3 layer, leading to an increased drain-source current (I_{DS}) due to the enhanced channel conductance. Conversely, when a negative gate bias was applied, the opposite process was achieved, resulting in an "erasing" action (*40*, *41*).

By exploiting this floating gate effect, biological synaptic functions were emulated upon applying $V_D = -60$ V combined with eight stimulus V_G pulses. The writing and erasing operations can be reversibly controlled by the polarity of the gate bias, as plotted in Fig. 2 (G and H), respectively. The excitatory postsynaptic current (PSC; measured as I_{DS}) could be triggered by applying a positive V_G stimulus (100 V, 12 s). Once the stimulus was ceased, the PSC raised to approximately 0.3 mA. Logically, one of the most important neuronal functions is the STP-to-LTP transition, which was observed after applying in series an increased number of stimuli, from one to eight, thereby enhancing the intensity of PSC from 0.3 to 0.6 mA. Another key synaptic function in neuromorphic systems is represented by the changes in the synaptic weight modulated by the spike timing to master STDP. The PSC response to one stimulus having a width ranging from 6 to 24 s (fig. S2, A and B) shows that a longer

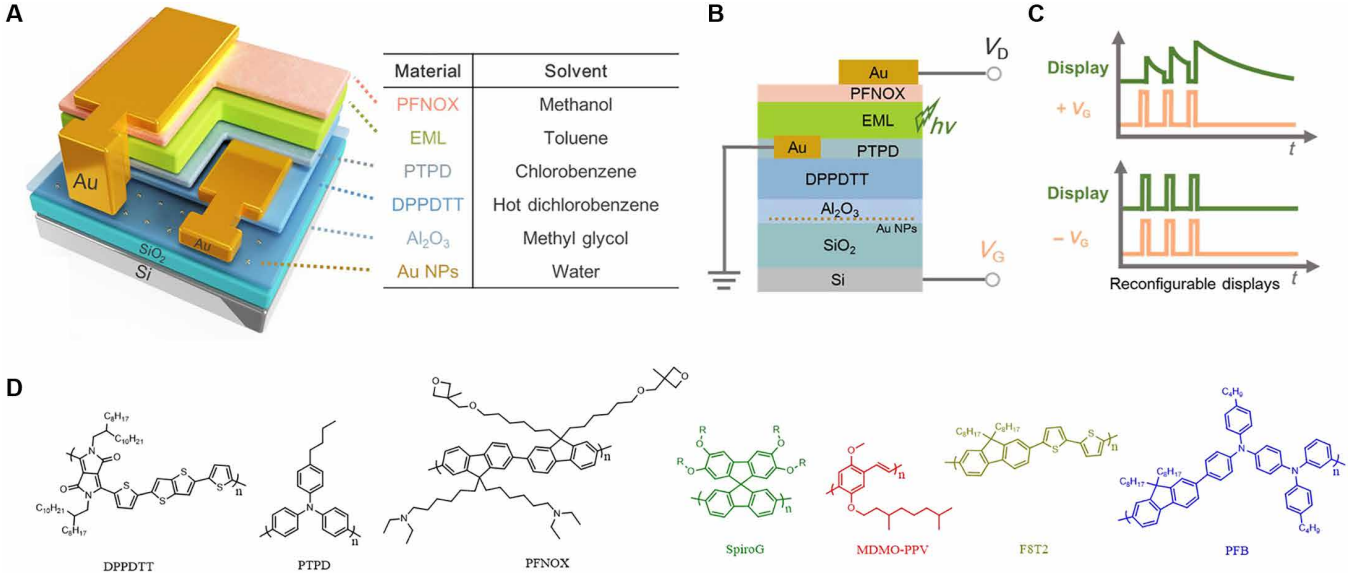

Fig. 1. Schematic images of the device structure and chemical structures. (**A**) Aerial view: Device structure of LAOLETs. (**B**) Corresponding schematic cross section (front view) of LAOLETs. (**C**) Schematic demonstrating the reconfigurable displays. (**D**) Chemical structures of DPPDTT, PTPD, PFNOX, and the four EMLs, i.e., SpiroG, MDMO-PPV, F8T2, and PFB.

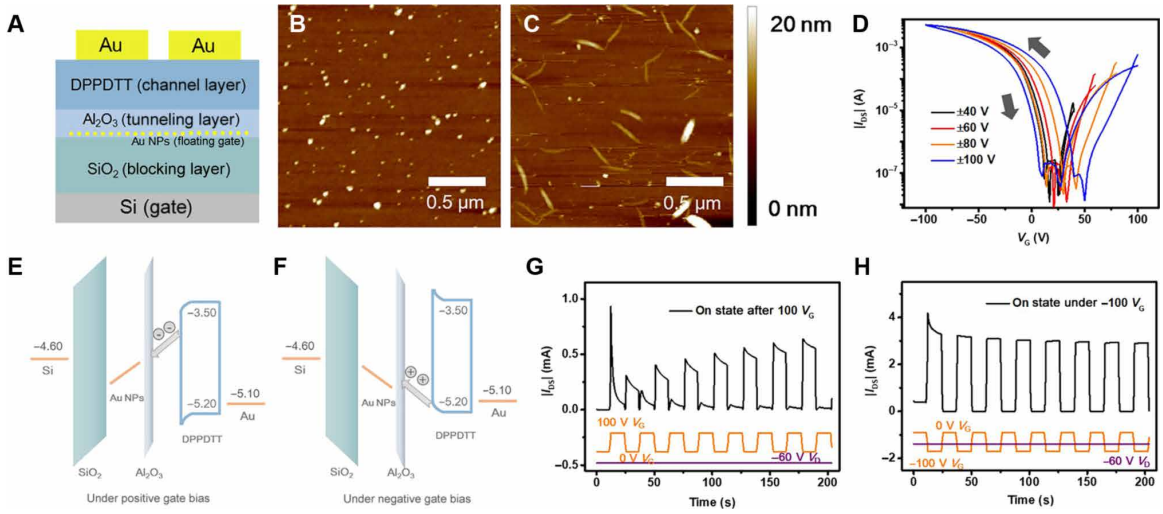

Fig. 2. Device structure and working mechanisms of NFGTs. (**A**) Scheme of the multilayered NFGTs device. AFM topographical images of Au NPs (**B**) before and (**C**) after Al_2O_3 thin-film coverage. *Z* scales = 20 nm. (**D**) Transfer hysteresis curves of NFGTs under different V_G sweeping range. Schematic energy band diagrams and charge flow of the NFGT device during (**E**) writing and (**F**) erasing operation. Time-dependent measurement of devices with eight positive and negative V_G spiked as (**G**) writing and (**H**) erasing operations, respectively. Orange and purple lines represent the real-time V_G and V_D, respectively.

stimulus width resulted in greater PSC values with longer retention time. In addition, the erasing of PSC in synaptic device could also be mimicked. A typical erasing current at an amplitude of 0.1 μA could be triggered by a negative V_G spike (−100 V, 12 s), providing a superior writing/erasing current ratio ($I_{W/E}$) of 10^3 (fig. S2C). Apart from postsynaptic depression, there is an increasing current at an amplitude of 1 mA as a result of each negative V_G spike, revealing the "on state" of the devices. Starting from the third negative V_G spike, such an on-state current maintained an amplitude of 3 mA because of the charge saturation absorption of Au NPs, offering a mean to power light emission. The results of this real-time writing/erasing process provide unambiguous evidence that NGFTs can be turned on both "after positive gate voltage" and "under negative gate voltage."

Fabrication and work mechanism of LAOLETs

To impart a synaptic function to light-emitting devices, green long afterglow OLETs (G-LAOLETs) were fabricated and characterized by using SpiroG as light-emitting material. The optical images of the devices are displayed in Fig. 3A. Aiming at superimposing via solution processing of four layers of different functionalized polymers, we have selected three conjugate polymers soluble in nonpolar solvents with specific order of solvent dissolvability, being specifically hot dichlorobenzene, chlorobenzene, and toluene, respectively, followed by the deposition of a final alcohol-soluble *n*-type polymer. AFM imaging of 2-μm by 2-μm regions of these films before and after soaking of the solvent from the upper layer was used to evaluate the quality of the layer-by-layer interface (fig. S3). The morphology of DPPDTT films before and after chlorobenzene soaking exhibited relatively smooth surface with a root square mean roughness (R_{RMS}) of about 1.1 nm. Differently, the morphology of PTPD film after soaking showed a slightly higher R_{RMS} of about 0.5 nm, when compared with its pristine film (with a R_{RMS} of about 0.2 nm), still confirming the ultrasmooth nature of the interface between HTL and EML. Expectedly, the R_{RMS} of the SpiroG film remained 0.2 nm after methanol soaking. The sharp interface between individual layers in the stack can be also observed from cross-sectional scanning electron microscopy (SEM) imaging of the G-LAOLETs (Fig. 3B), providing further confirmation of the viability of the used process for the controlled deposition of four stacked polymer layers. The thickness of films was determined from these SEM images and confirmed by profilometry (fig. S4A).

The energy levels of the polymers forming the multilayer structure and the working mechanism, including memory and display processes, are illustrated in Fig. 3 (C and D). As previously explained, when a suitable presynaptic voltage is applied to the gate terminal, electrons accumulating at interface between the tunneling layer and the channel layer can be injected into NFG and are stored, resulting in enhancement of the conductance of DPPDTT when the voltage stimulus is ceased. Predictably, an enhancement of the conductance of DPPDTT can be also attained upon applying a negative gate bias. However, for the light emission operation, a negative drain bias needs to be also applied. Hole carriers are injected from the source electrode to the channel layer and then transported to PTPD, while electron carriers are injected from the drain electrode to the PFNOX, leading to hole-electron carrier recombination in the light-emitting polymer and forming a uniform drain-shaped region of emission.

Characteristics of LAOLETs

Electrical and optical hysteresis transfer curves of G-LAOLETs are displayed in Fig. 4A. In addition, electrical and optical output curves of these devices are displayed fig. S5 (A and B), respectively. The maximum current and brightness of G-LAOLETs reached 3 mA and 2500 cd m^{-2} when V_D = −60 V and V_G = −100 V were applied. A saturation hole field-effect mobility of 0.25 cm^2 V^{-1} s^{-1} and an I_{on}/I_{off} ratio of 10^5 were also obtained. To demonstrate the reproductively of these devices, transfer curves of 10 G-LAOLETs from five batches are plotted in fig. S6. Similar to the NFGTs, the NFG-driven memory behavior was also observed in the G-LAOLETs, as evidenced by two distinct states in two sweeping directions. In the backward sweep direction, V_{Th} of devices was set at −2 V and light turn-on voltage (V_{on}) was set at 1 V, whereas in the forward sweep

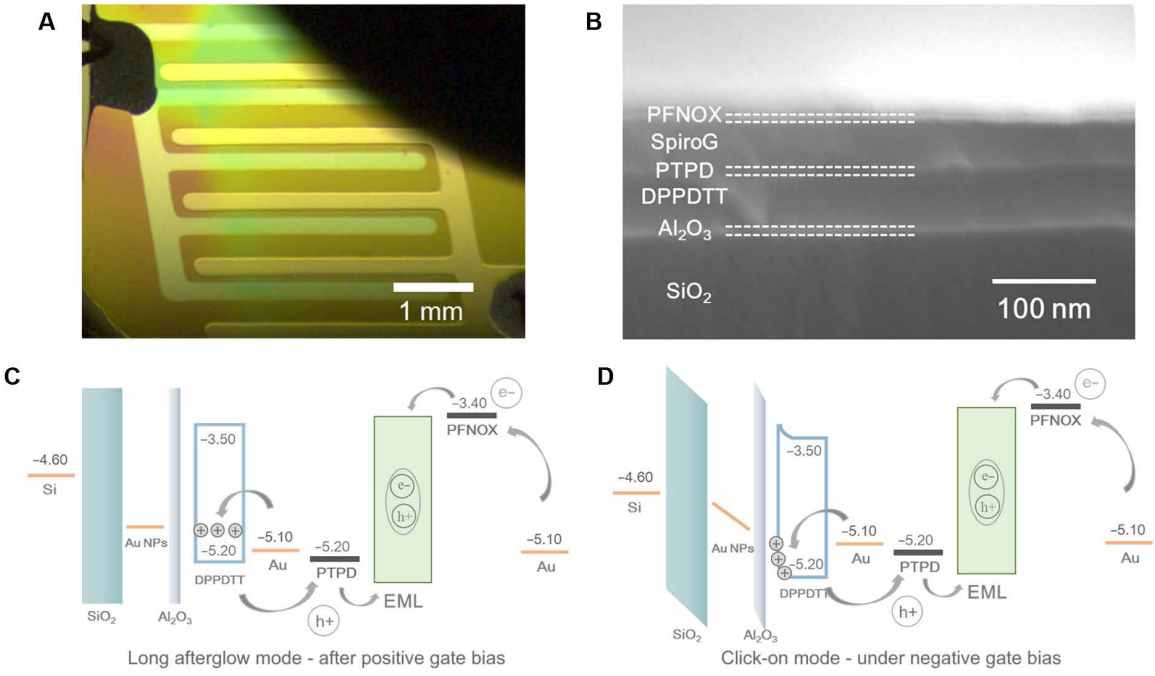

Fig. 3. LAOLETs and their working mechanisms. (**A**) Optical image of LAOLETs under light. (**B**) Cross-sectional SEM image of G-LAOLETs. LAOLET's working mechanisms: (**C**) long afterglow mode and (**D**) click-on mode.

direction, V_{Th} and V_{on} were set at −41 and −40 V, respectively. Both current and brightness memory window (ΔV_{Th} and ΔV_{on}) are calculated as ~40 V, allowing the devices to operate as memory displays.

To further elucidate the memory display properties of G-LAOLETs, electric time-dependent measurements of the device's intergraded brightness under V_D = −60 V upon varying V_G were carried out and displayed in Fig. 4 (B and C). Expectedly, exploiting the memory current to power the memory display, the device's postsynaptic brightness (PSB) featured a trend similar to the PSC in both writing/erasing operations. Analogous to the long afterglow phenomenon that has attracted quite some interests for applications in optical data storage, in vivo imaging, and anticounterfeiting (*42*, *43*), this time-resolved decay behavior of PSB can be exploited to achieve similar device functions, working as the "long afterglow mode." Initially, the device's PSC was about 4 μA, being too low to drive the light emission. Once a positive spike (V_G = 100 V, 12 s) stimulus finished, the PSC and PSB became measurable and were found to amount to 0.12 mA and 81 cd m^{-2}, respectively. Because DPPDTT is an ambipolar semiconductor with a narrow bandgap, when a positive V_G is applied, the hole carrier can inject from the source electrode to the lowest unoccupied molecular orbital level of DPPDTT. For practical applications, this current peak can be inhibited by exploiting a wide bandgap polymer as channel material. After repeating these spikes eight times, the PSC and PSB have grown, reaching 0.24 mA and 142 cd m^{-2}, hence demonstrating that a greater current and light emission could be simultaneously reached by repeating the signal input, also indicating that the lifetime of this long afterglow emission is limited by the lifetime of PSC. The mechanism ruling this process consisted in the stepwise enhancement of the amount of electrons being trapped into the NFG upon increasing the number of spikes. Figure 4D shows the PSC and PSB response to a single stimulus having a width ranging from 6 to 24 s. According to the fitting (fig. S4B), after having applied a stimulus of V_G = 100 V for 6 s, a L_0 of 18 cd m^{-2} with a lifetime (τ_l) of 12.8 s was obtained. Upon the gradual increase of the stimulus width to 12 and 24 s, enhanced L_0 to 60 and 127 cd m^{-2} with prolonged τ_l to 14.1 and 17.2 s of PSB were observed. On the other hand, PSC and PSB of devices can be inhibited by one negative spike (V_G = −100 V, 12 s), decreasing to 0.1 μA and 0 cd m^{-2}, hence revealing an $I_{W/E}$ of 10^3. Apparently, the current intensity of >1 mA under each negative V_D spikes could drive the light emission in the devices, defining another work mode as "click-on." According to the time-dependent measurements shown in Fig. 4E, although the current exhibited a slight decay upon applying a negative gate voltage, a stable on-state current of ~1 mA accompanied with a stable brightness of ~300 cd m^{-2} was observed after 150 s of continuous application of a negative V_G, due to the nearly saturated absorption of NFG. These results provide evidence that two different display operating modes, i.e., long afterglow and click-on, can be achieved simultaneously in the same display unit by using positive gate voltage and negative gate voltage spike, respectively. The optical image of the devices including the initial state and the two working modes in the dark are presented in Fig. 4F.

Devices capable to emit light with three different colors were fabricated by using different light-emitting polymers as active components. In particular, we used MDMO-PPV for red (R-LAOLET), F8T2 for yellow (Y-LAOLET), and PFB for blue (B-LAOLET). Electric and optical hysteresis transfer curves of R-, Y-, and B-LAOLETs are measured (fig. S7, A to C). All these devices exhibited a maximum current of around 3 mA and I_{on}/I_{off} ratios reaching 10^5. Upon applying V_G = −100 V and V_D = −60 V to the LAOLETs, we observed maximum brightness values of 493, 1666, and 66 cd m^{-2} for red, yellow, and blue light-emitting devices, respectively (Fig. 4G). At the same time, all these LAOLETs exhibited approximately ΔV_{Th}

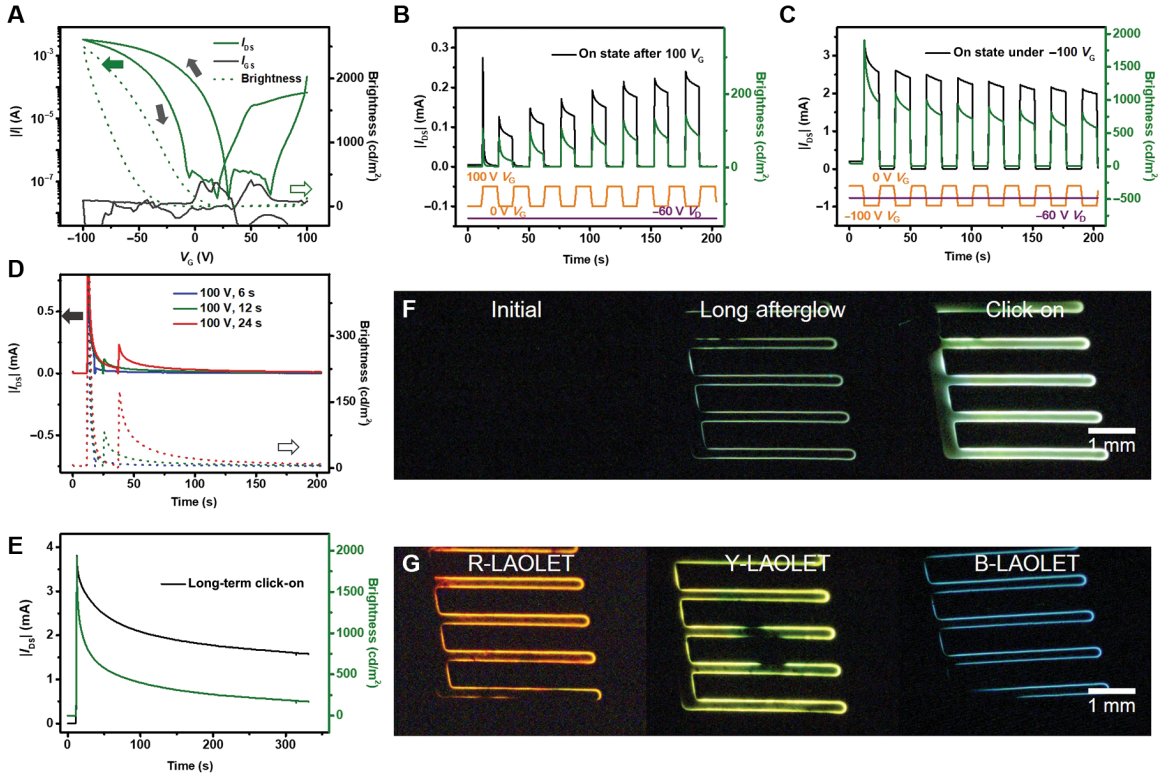

Fig. 4. Electrical and optical characterization of LAOLETs. (**A**) Electric and optical transfer curves of G-LAOLETs. The solid lines represent the electric curves, while the dotted lines represent the brightness curves. The time-dependent electric and optical measurement of devices with eight positive and negative gate spiked was used as (**B**) long afterglow mode and (**C**) click-on mode, respectively. Orange and purple lines represent the real-time gate and drain voltage, respectively. (**D**) Time-resolved electrical and optical decay curves of G-LAOLETs after the application of V_G = 100 V with different stimulus width. (**E**) Stabilized measurement of G-LAOLETs when negative V_G was applied continuously. (**F**) Optical image of LAOLETs under the same V_D = −60 V and different V_G conditions: initial state of device, under dark, and V_G = 0; long afterglow mode, after 20-s spiked V_G = 100 V; and click-on mode, under spiked V_G = −100 V. (**G**) Optical images of R-, Y-, and B-LAOLETs when V_D = −60 V and V_G = −100 V were applied.

and ΔV_{on} of ~30 V and $I_{W/E}$ of ~10^4, indicating that the synaptic behavior was retained regardless of the used light-emitting polymers. The electroluminescence peaks of the R-, Y-, B-, and G-LAOLETs were located at 603, 550, 450, and 542 nm, respectively (fig. S7D). To further evaluate the influence of the light-emitting material on memory display properties, electric and optical time-dependent measurements of full-color LAOLETs under V_D = −60 V upon varying V_G were carried out and displayed in figs. S8 to S10. It is clear that two different work modes were realized successfully whatever the light-emitting materials were using. These results demonstrate that LAOLETs with optimized color emission could be achieved by simply selecting the ideal light-emitting materials.

Toward long afterglow sensors

Pressure sensing represents a crucial input that needs to be embedded in intelligent bionic systems, especially because flexible and wearable pressure sensors can satisfy the needs of human motion detection for health and disease diagnosis. Electrically conductive polymer nanocomposites have been widely reported as a piezo-resistive sensor. Hence, toward processing long afterglow sensors, a graphene sponge was selected because of their advantages of low-cost, environmentally friendly, and simple fabrication (*44*). The optical image and current-voltage relation (*I*-*V*) characterized curves of the graphene sponge are presented (fig. S11). When a pressure of ca. 6 kPa was exerted to the graphene sponge, the pressure sensor was drastically transformed from a high resistant state to a low resistant state. As a proof-of-concept assessment of a practical application of the long afterglow device, long afterglow pressure sensors were fabricated by integrating two units (Fig. 5A and fig. S12), a graphene sponge as a pressure sensor component and a G-LAOLET unit fabricated as described above. Real-time measurement of this long afterglow pressure sensor is displayed in Fig. 5B upon applying a V_G of 120 V. The orange, black, and green lines correspond to I_{GS}, I_{DS}, and brightness, respectively. Initially, the pressure sensor resistance was much greater than the setting resistance. When a pressure was exerted on the device, I_{GS} increased to 0.02 mA, and the resistance of total circuit (which corresponds to the sum of the setting and the pressure sensor resistance) was calculated as 6 megohm. Correspondingly, the voltage dropped on G-LAOLETs could be emulated as 100 V, leading to long afterglow emission after ceasing the pressure signal input. This long afterglow emission could also be enhanced by repeating the pressure signal input. Another operating mode was also achieved upon applying a V_G of −120 V. Light emission of device was observed when each pressure signal input was applied (Fig. 5C). In the future, upon changing the responsive units, different kinds of long afterglow sensors capable to respond to diverse stimuli can be used for light, thermal, sound, and biomolecular sensing in new active displays (*45*).

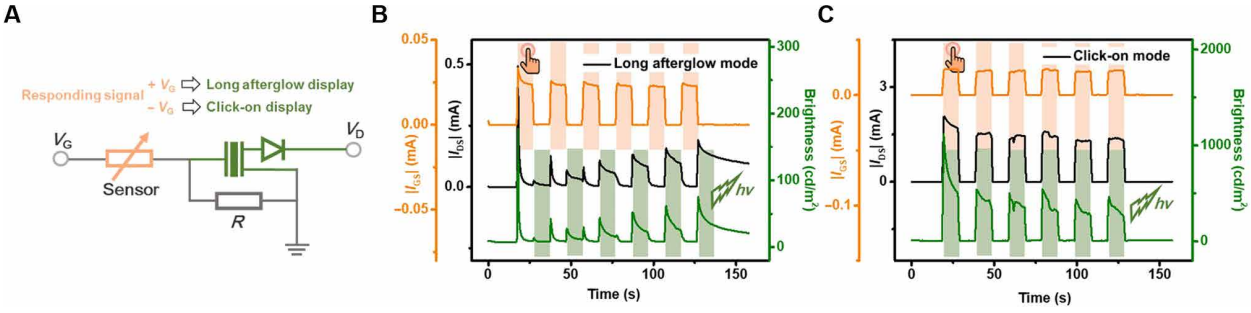

Fig. 5. Long afterglow pressure sensor. (**A**) Equivalent electrical circuit integrating the pressure sensor function in a G-LAOLET. *R* is a setting resistance of 5 megohm. Real-time measurement of long afterglow pressure sensor upon applying a V_G of (**B**) 120 V and (**C**) −120 V.

DISCUSSION

In summary, we have reported the fabrication of unprecedented electrical spiked LAOLETs by assembling on a Si/SiO_2 wafer by successive spin-coating depositions a multilayered structure comprising Au NPs as an NFG layer coated with an insulating Al_2O_3 tunneling barrier supporting four different functionalized polymer layers, which act as a channel, hole transport, light emission, and electron transport layer, respectively. By using SpiroG as light-emitting material, G-LAOLETs with a maximum brightness of 2500 cd m^{-2} and an I_{on}/I_{off} ratio of 10^5 were realized. After applying a positive gate spike as a presynaptic stimulus, a long afterglow display of 81 cd m^{-2} with a lifetime of 14.08 s was attained. The PSB of devices can be enhanced to 142 cd m^{-2} by repeating the stimulus. At the same time, the lifetime of PSB could be prolonged to 17.17 s by increasing stimulus width to 24 s. Importantly, another operating mode, displaying a prompt light emission under each negative gate spiked, was also observed in the same device. In light of these unique characteristics, our LAOLETs can find application as reconfigurable displays. Furthermore, by exploiting four commercially available semiconducting polymers as light-emissive layers, full-color LAOLETs ranged in whole visible light were achieved with approximately ΔV_{Th} and ΔV_{on} of ~30 V and $I_{W/E}$ of ~10^3, respectively. As a proof of concept, force-triggered long afterglow emission was observed in pressure sensor–integrated LAOLETs, demonstrating that our LAOLETs can respond to bionic stimulus for artificial sensory–related synaptic display in tomorrow's smart optoelectronics.

MATERIALS AND METHODS

Materials

Au NP solution, octylphosphonic acid, SpiroG, MDMO-PPV, F8T2, and PFB were purchased from Sigma-Aldrich. PFNOX was purchased from Lumtec. DPPDTT [weight-average molecular weight (M_W) > 100 K] and PTPD (M_W ~ 80 K) were purchased from 1-Material. All the materials were used as received, without any further purification.

Preparation of solutions

Al_2O_3 precursor solution

$Al(NO_3)_3{\cdot}9H_2O$ was dissolved in 2-methoxyethanol at a concentration of 0.1 M and stirred at room temperature overnight.

DPPDTT solution

Forty milligrams of DPPDTT was dissolved in 10 ml of dichlorobenzene and then stirred at 80°C overnight. The solutions were heated at 150°C for 30 min before being spin-coated.

PTPD solution

Sixty milligrams of PTPD was dissolved in 10 ml of chlorobenzene and then stirred at 80°C overnight.

Solution of the light-emitting polymers

Eighty milligrams of SpiroG, MDMO-PPV, F8T2, and PFB was dissolved in 10 ml of toluene and then stirred at 80°C overnight.

PFNOX solution

Ten milligrams of PFNOX was dissolved in 5 ml of methanol and 50 μl of acetic acid and then stirred at 80°C overnight. The solutions were filtered through a 0.22-μm polytetrafluoroethylene filter before being spin-coated.

Device fabrication

Devices were fabricated on the substrates of n^{++} Si as bottom gate coated with 230 nm of thermally grown SiO_2 as the gate dielectric (IPMS Fraunhofer Institute). The Si/SiO_2 substrates were cleaned with water, acetone, and alcohol in sequence and dried under N_2 flow. The cleaned substrates were further treated with ultraviolet ozone for 20 min. Au NP solution was spin-coated at 800 rpm for 2 min on the silicon wafer followed with 0.1 M Al_2O_3 precursor solution spin-coated at 3000 rpm for 45 s. Subsequently, the substrate was dried at 150°C for 5 min and baked at 360°C for 30 min. The substrates were soaked in 0.05 M octylphosphonic acid solution overnight before being used. A channel layer with a thickness of 50 nm was spin-coated on substrates from hot DPPDTT solution. For NFGTs, interdigitated Au electrodes (40 nm) were deposited on the DPPDTT film through shadow masks. For LAOLETs, source electrode (Au; 50 nm) was evaporated on the DPPDTT film through shadow masks. Subsequently, the hole transport layer with a thickness of 10 nm was spun from PTPD solution, followed by a thermal annealing at 150°C for 20 min. EML of different color with a thickness of 45 nm was spun from the corresponding emitting solution, followed by thermal annealing at 130°C for 20 min. Electron transport layer with a thickness of 10 nm was spun from PFNOX solution, followed by a thermal annealing at 130°C for 20 min. Last, the drain electrode (Au; 35 nm) was deposited through shadow masks. The width (*W*) and length (*L*) of the channel in LAOLETs amounted to 27 mm and 200 μm, respectively, whereas the emission area was defined as 4.22 mm^2.

Pressure sensor fabrication

The graphene ethanol solution was prepared by low-cost and scalable wet chemical electrochemical exfoliation approaches following previously report procedures (*46*). A melamine sponge with a size

of 15 mm by 15 mm by 5 mm was soaked in 3 weight % graphene solution overnight. After the removal of the solution in the vacuum chamber, two iron plates were tapped on the top and bottom of the graphene-absorbed sponge for connecting.

Characterization

Devices were characterized in a dry and nitrogen-filled glove box. The electrical characteristics and basic synaptic functions were measured by a semiconductor parameter analyzer (Keithley, 2636). Irradiation intensity of the device was measured by a photodiode (Hamamatsu, S3204-08), which have been previously calibrated by a luminance meter (Konica minolta, LS-100). The electroluminescence spectrum of OLETs was measured by Ocean Optics FLAME-S. AFM images were recorded with a Bruker Dimension Icon setup operating under ambient conditions, in tapping mode. SEM images were taken with Quanta FEG 250 from FEI Company. The thickness of the films was determined by the Alpha-Sep IQ Surface Profiler.

SUPPLEMENTARY MATERIALS

Supplementary material for this article is available at https://science.org/doi/10.1126/sciadv.abq4824

REFERENCESAND NOTES

1. Z. Wu, Y. Liu, E. Guo, G. Darbandy, S.-J. Wang, R. Hübner, A. Kloes, H. Kleemann, K. Leo, Efficient and low-voltage vertical organic permeable base light-emitting transistors. *Nat. Mater.* **20**, 1007–1014 (2021).
2. M. A. McCarthy, B. Liu, E. P. Donoghue, I. Kravchenko, D. Y. Kim, F. So, A. G. Rinzler, Low-voltage, low-power, organic light-emitting transistors for active matrix displays. *Science* **332**, 570–573 (2011).
3. R. Capelli, S. Toffanin, G. Generali, H. Usta, A. Facchetti, M. Muccini, Organic light-emitting transistors with an efficiency that outperforms the equivalent light-emitting diodes. *Nat. Mater.* **9**, 496–503 (2010).
4. M. U. Chaudhry, K. Muhieddine, R. Wawrzinek, J. Sobus, K. Tandy, S.-C. Lo, E. B. Namdas, Organic light-emitting transistors: Advances and perspectives. *Adv. Funct. Mater.* **30**, 1905282 (2020).
5. L. Hou, X. Zhang, G. F. Cotella, G. Carnicella, M. Herder, B. M. Schmidt, M. Patzel, S. Hecht, F. Cacialli, P. Samorì, Optically switchable organic light-emitting transistors. *Nat. Nanotechnol.* **14**, 347–353 (2019).
6. Y. Chen, H. Wang, Y. Yao, Y. Wang, C. Ma, P. Samorì, Synaptic plasticity powering long-afterglow organic light-emitting transistors. *Adv. Mater.* **33**, 2103369 (2021).
7. S. Wang, J. Xu, W. Wang, G.-J. N. Wang, R. Rastak, F. Molina-Lopez, J. W. Chung, S. Niu, V. R. Feig, J. Lopez, T. Lei, S.-K. Kwon, Y. Kim, A. M. Foudeh, A. Ehrlich, A. Gasperini, Y. Yun, B. Murmann, J. B.-H. Tok, Z. Bao, Skin electronics from scalable fabrication of an intrinsically stretchable transistor array. *Nature* **555**, 83–88 (2018).
8. Y. Ma, N. Liu, L. Li, X. Hu, Z. Zou, J. Wang, S. Luo, Y. Gao, A highly flexible and sensitive piezoresistive sensor based on MXene with greatly changed interlayer distances. *Nat. Commun.* **8**, 1207 (2017).
9. T. Yamada, Y. Hayamizu, Y. Yamamoto, Y. Yomogida, A. Izadi-Najafabadi, D. N. Futaba, K. Hata, A stretchable carbon nanotube strain sensor for human-motion detection. *Nat. Nanotechnol.* **6**, 296–301 (2011).
10. S. Lee, A. Reuveny, J. Reeder, S. Lee, H. Jin, Q. Liu, T. Yokota, T. Sekitani, T. Isoyama, Y. Abe, Z. Suo, T. Someya, A transparent bending-insensitive pressure sensor. *Nat. Nanotechnol.* **11**, 472–478 (2016).
11. Q.-B. Zhu, B. Li, D.-D. Yang, C. Liu, S. Feng, M.-L. Chen, Y. Sun, Y.-N. Tian, X. Su, X.-M. Wang, S. Qiu, Q.-W. Li, X.-M. Li, H.-B. Zeng, H.-M. Cheng, D.-M. Sun, A flexible ultrasensitive optoelectronic sensor array for neuromorphic vision systems. *Nat. Commun.* **12**, 1798 (2021).
12. Y. Yao, Q. Ou, K. Wang, H. Peng, F. Fang, Y. Shi, Y. Wang, D. I. Asperilla, Z. Shuai, P. Samorì, Supramolecular engineering of charge transfer in wide bandgap organic semiconductors with enhanced visible-to-NIR photoresponse. *Nat. Commun.* **12**, 3667 (2021).
13. Y. Lee, J. Y. Oh, W. Xu, O. Kim, T. R. Kim, J. Kang, Y. Kim, D. Son, J. B.-H. Tok, M. J. Park, Z. Bao, T.-W. Lee, Stretchable organic optoelectronic sensorimotor synapse. *Sci. Adv.* **4**, eaat7387 (2018).
14. W. Y. Chen, X. Jiang, S. N. Lai, D. Peroulis, L. Stanciu, Nanohybrids of a MXene and transition metal dichalcogenide for selective detection of volatile organic compounds. *Nat. Commun.* **11**, 1302 (2020).
15. N. Turetta, M.-A. Stoeckel, R. F. Oliveira, F. Devaux, A. Greco, C. Cendra, S. Gullace, M. Gicevičius, B. Chattopadhyay, J. Liu, G. Schweicher, H. Sirringhaus, A. Salleo, M. Bonn, E. H. G. Backus, Y. H. Geerts, P. Samorì, High-performance humidity sensing in π-conjugated molecular assemblies through the engineering of electron/proton transport and device interfaces. *J. Am. Chem. Soc.* **144**, 2546–2555 (2022).
16. F. Cicoira, M. Sessolo, O. Yaghmazadeh, J. A. DeFranco, S. Y. Yang, G. G. Malliaras, Influence of device geometry on sensor characteristics of planar organic electrochemical transistors. *Adv. Mater.* **22**, 1012–1016 (2010).
17. P. Escobedo, M. D. Fernández-Ramos, N. López-Ruiz, O. Moyano-Rodríguez, A. Martínez-Olmos, I. M. Pérez de Vargas-Sansalvador, M. A. Carvajal, L. F. Capitán-Vallvey, A. J. Palma, Smart facemask for wireless CO_2 monitoring. *Nat. Commun.* **13**, 72 (2022).
18. Y. Song, J. Min, Y. Yu, H. Wang, Y. Yang, H. Zhang, W. Gao, Wireless battery-free wearable sweat sensor powered by human motion. *Sci. Adv.* **6**, eaay9842 (2020).
19. P.-F. Wang, X. Lin, L. Liu, Q.-Q. Sun, P. Zhou, X.-Y. Liu, W. Liu, Y. Gong, D. W. Zhang, A semi-floating gate transistor for low-voltage ultrafast memory and sensing operation. *Science* **341**, 640–643 (2013).
20. S.-T. Han, Y. Zhou, C. Wang, L. He, W. Zhang, V. A. L. Roy, Layer-by-layer-assembled reduced graphene oxide/gold nanoparticle hybrid double-floating-gate structure for low-voltage flexible flash memory. *Adv. Mater.* **25**, 872–877 (2013).
21. W. Shi, Y. Guo, Y. Liu, When flexible organic field-effect transistors meet biomimetics: A prospective view of the internet of things. *Adv. Mater.* **32**, 1901493 (2020).
22. C. Liu, X. Yan, X. Song, S. Ding, D. W. Zhang, P. Zhou, A semi-floating gate memory based on van der Waals heterostructures for quasi-non-volatile applications. *Nat. Nanotechnol.* **13**, 404–410 (2018).
23. E. J. Fuller, S. T. Keene, A. Melianas, Z. Wang, S. Agarwal, Y. Li, Y. Tuchman, C. D. James, M. J. Marinella, J. J. Yang, A. Salleo, A. A. Talin, Parallel programming of an ionic floating-gate memory array for scalable neuromorphic computing. *Science* **364**, 570–574 (2019).
24. I. Krauhausen, D. A. Koutsouras, A. Melianas, S. T. Keene, K. Lieberth, H. Ledanseur, R. Sheelamanthula, A. Giovannitti, F. Torricelli, I. Mcculloch, P. W. M. Blom, A. Salleo, Y. van de Burgt, P. Gkoupidenis, Organic neuromorphic electronics for sensorimotor integration and learning in robotics. *Sci. Adv.* **7**, eabl5068 (2021).
25. F. A. Viola, J. Barsotti, F. Melloni, G. Lanzani, Y.-H. Kim, V. Mattoli, M. Caironi, A sub-150-nanometre-thick and ultraconformable solution-processed all-organic transistor. *Nat. Commun.* **12**, 5842 (2021).
26. F. Molina-Lopez, T. Z. Gao, U. Kraft, C. Zhu, T. Öhlund, R. Pfattner, V. R. Feig, Y. Kim, S. Wang, Y. Yun, Z. Bao, Inkjet-printed stretchable and low voltage synaptic transistor array. *Nat. Commun.* **10**, 2676 (2019).
27. S. Chu, W. Chen, Z. Fang, X. Xiao, Y. Liu, J. Chen, J. Huang, Z. Xiao, Large-area and efficient perovskite light-emitting diodes via low-temperature blade-coating. *Nat. Commun.* **12**, 147 (2021).
28. H. Yuk, B. Lu, S. Lin, K. Qu, J. Xu, J. Luo, X. Zhao, 3D printing of conducting polymers. *Nat. Commun.* **11**, 1604 (2020).
29. B. E. Droguet, H.-L. Liang, B. Frka-Petesic, R. M. Parker, M. F. L. De Volder, J. J. Baumberg, S. Vignolini, Large-scale fabrication of structurally coloured cellulose nanocrystal films and effect pigments. *Nat. Mater.* **21**, 352–358 (2021).
30. V. Pecunia, M. Nikolka, A. Sou, I. Nasrallah, A. Y. Amin, I. McCulloch, H. Sirringhaus, Trap healing for high-performance low-voltage polymer transistors and solution-based analog amplifiers on foil. *Adv. Mater.* **29**, 1606938 (2017).
31. A. C. Arias, J. D. MacKenzie, I. McCulloch, J. Rivnay, A. Salleo, Materials and applications for large area electronics: Solution-based approaches. *Chem. Rev.* **110**, 3–24 (2010).
32. S. Lee, M.-J. Choi, G. Sharma, M. Biondi, B. Chen, S.-W. Baek, A. M. Najarian, M. Vafaie, J. Wicks, L. K. Sagar, S. Hoogland, F. P. G. de Arquer, O. Voznyy, E. H. Sargent, Orthogonal colloidal quantum dot inks enable efficient multilayer optoelectronic devices. *Nat. Commun.* **11**, 4814 (2020).
33. K. Muhieddine, M. Ullah, B. N. Pal, P. Burn, E. B. Namdas, All solution-processed, hybrid light emitting field-effect transistors. *Adv. Mater.* **26**, 6410–6415 (2014).
34. K. Muhieddine, M. Ullah, F. Maasoumi, P. L. Burn, E. B. Namdas, Hybrid area-emitting transistors: Solution processable and with high aperture ratios. *Adv. Mater.* **27**, 6677–6782 (2015).
35. H. Zhou, Y. Zhang, C.-K. Mai, S. D. Collins, T.-Q. Nguyen, G. C. Bazan, A. J. Heeger, Conductive conjugated polyelectrolyte as hole-transporting layer for organic bulk heterojunction solar cells. *Adv. Mater.* **26**, 780–785 (2014).
36. B. R. Lee, J. C. Yu, J. H. Park, S. Lee, C.-K. Mai, B. Zhao, M. S. Wong, E. D. Jung, Y. S. Nam, S. Y. Park, D. D. Nuzzo, J. Y. Kim, S. D. Stranks, G. C. Bazan, H. Choi, M. H. Song, R. H. Friend, Conjugated polyelectrolytes as efficient hole transport layers in perovskite light-emitting diodes. *ACS Nano* **12**, 5826–5833 (2018).
37. H. Chen, X. Xing, J. Miao, C. Zhao, M. Zhu, J. Bai, Y. He, H. Meng, Highly efficient flexible organic light emitting transistor based on high-*k* polymer gate dielectric. *Adv. Opt. Mater.* **8**, 1901651 (2020).
38. H. Gao, Z. Miao, Z. Qin, J. Yang, T. Wang, C. Gao, H. Dong, W. Hu, Redistributed current density in lateral organic light-emitting transistors enabling uniform area emission with good stability and arbitrary tunability. *Adv. Mater.* **34**, 2108795 (2021).

39. M. Prosa, E. Benvenuti, D. Kallweit, P. Pellacani, M. Toerker, M. Bolognesi, L. Lopez-Sanchez, V. Ragona, F. Marabelli, S. Toffanin, Organic light-emitting transistors in a smart-integrated system for plasmonic-based sensing. *Adv. Funct. Mater.* **31**, 2104927 (2021).
40. A. Sebastian, M. L. Gallo, R. Khaddam-Aljameh, E. Eleftheriou, Memory devices and applications for in-memory computing. *Nat. Nanotechnol.* **15**, 529–544 (2020).
41. V. K. Sangwan, M. C. Hersam, Neuromorphic nanoelectronic materials. *Nat. Nanotechnol.* **15**, 517–528 (2020).
42. Z. An, C. Zheng, Y. Tao, R. Chen, H. Shi, T. Chen, Z. Wang, H. Li, R. Deng, X. Liu, W. Huang, Stabilizing triplet excited states for ultralong organic phosphorescence. *Nat. Mater.* **14**, 685–690 (2015).
43. J.-H. Wei, J.-F. Liao, L. Zhou, J.-B. Luo, X.-D. Wang, D.-B. Kuang, Indium-antimony-halide single crystals for high-efficiency white-light emission and anti-counterfeiting. *Sci. Adv.* **7**, eabg3989 (2021).
44. J. Zhao, W. Ren, H.-M. Cheng, Graphene sponge for efficient and repeatable adsorption and desorption of water contaminations. *J. Mater. Chem.* **22**, 20197–20202 (2012).
45. K. Ditte, T. A. N. Le, O. Ditzer, D. I. S. Bojorquez, S. Chae, M. Bachmann, L. Baraban, F. Lissel, Rapid detection of SARS-CoV-2 antigens and antibodies using OFET biosensors based on a soft and stretchable semiconducting polymer. *ACS Biomater. Sci. Eng.* 10.1021/acsbiomaterials.1c00727 (2021).
46. Z. Liu, H. Qiu, S. Fu, C. Wang, X. Yao, A. G. Dixon, S. Campidelli, E. Pavlica, G. Bratina, S. Zhao, L. Rondin, J.-S. Lauret, A. Narita, M. Bonn, K. Müllen, A. Ciesielski, H. I. Wang, P. Samorì, Solution-processed graphene–nanographene van der waals heterostructures for photodetectors with efficient and ultralong charge separation. *J. Am. Chem. Soc.* **143**, 17109–17116 (2021).
47. R. A. Abumosa, B. A. Al-Asbahi, M. S. AlSalhi, Optical properties and amplified spontaneous emission of novel MDMO-PPV/C500 hybrid. *Polymers* **9**, 71 (2017).
48. P. A. Levermore, R. Jin, X. Wang, J. C. de Mello, D. D. C. Bradley, Organic light-emitting diodes based on poly(9,9-dioctylfluorene-co -bithiophene) (F8T2). *Adv. Funct. Mater.* **19**, 950–957 (2009).
49. C. E. Finlayson, A. D. Whitney, Photophysical studies of poly-isocyanopeptide based photovoltaic blends. *J. Phys. D Appl. Phys.* **43**, 095501 (2010).
50. Z. Zhang, W. Wang, Y. Jiang, Y.-X. Wang, Y. Wu, J.-C. Lai, S. Niu, C. Xu, C.-C. Shih, C. Wang, H. Yan, L. Galuska, N. Prine, H.-C. Wu, D. Zhong, G. Chen, N. Matsuhisa, Y. Zheng, Z. Yu, Y. Wang, R. Dauskardt, X. Gu, J. B.-H. Tok, Z. Bao, High-brightness all-polymer stretchable LED with charge-trapping dilution. *Nature* **603**, 624–630 (2022).
51. A. Ablat, A. Kyndiah, A. Bachelet, K. Takimiya, L. Hirsch, S. Fasquel, M. Abbas, Low optical turn-on voltage in solution processed hybrid light emitting transistor. *Appl. Phys. Lett.* **115**, 023301 (2019).
52. Y. J. Park, A. Song, B. Walker, J. H. Seo, K.-B. Chung, Hybrid ZnON–organic light emitting transistors with low threshold voltage <5 V. *Adv. Opt. Mater.* **7**, 1801290 (2019).
53. Y. Hu, L. Song, S. Zhang, Y. Lv, J. Lin, X. Guo, X. Liu, Improving the efficiency of multilayer organic light-emitting transistors by exploring the hole blocking effect. *Adv. Mater. Interfaces* **7**, 2000657 (2020).
54. V. Ahmad, J. Sobus, F. Bencheikh, M. Mamada, C. Adachi, S.-C. Lo, E. B. Namdas, High EQE and high brightness solution-processed TADF light-emitting transistors and OLEDs. *Adv. Opt. Mater.* **8**, 2000554 (2020).
55. D. Yuan, M. A. Awais, V. Sharapov, X. Liu, A. Neshchadin, W. Chen, M. Bera, L. Yu, Foldable semi-ladder polymers: Novel aggregation behavior and high-performance solution-processed organic light-emitting transistors. *Chem. Sci.* **11**, 11315–11321 (2020).
56. D. Yuan, M. A. Awais, V. Sharapov, X. Liu, A. Neshchadin, W. Chen, L. Yu, Highly emissive semi-ladder-type copolymers, aggregation state, and solution-processed organic light-emitting transistor. *Chem. Mater.* **11**, 4672–4680 (2020).
57. D. Yuan, M. A. Awais, V. Sharapov, X. Liu, A. Neshchadin, W. Chen, L. Yu, Synergy between photoluminescence and charge transport achieved by finely tuning polymeric backbones for efficient light-emitting transistor. *J. Am. Chem. Soc.* **143**, 5239–5246 (2021).

Acknowledgments

Funding: We acknowledge funding from the Agence Nationale de la Recherche through the Interdisciplinary Thematic Institute SysChem via the IdEx Unistra (ANR-10-IDEX-0002) within the program Investissement d'Avenir, the International Center for Frontier Research in Chemistry (icFRC), the Institut Universitaire de France (IUF), the EU-ERC project SUPRA2DMAT (GA-833707) and the Graphene Flagship Core 3 project (GA-881603), the PROSPECT project funded by the FLAG-ERA programme, the European Union, and the Agence Nationale de la Recherche (ANR) (GA no. ANR-19-GRF1-0005-02) and the Chinese Scholarship Council. **Author contributions:** P.S. and Y.C. conceived the experiments. Y.C. fabricated the LAOLETs and performed the measurements. H.W., F.L., and V.M.-G. performed the deposition of NFGTs, fabrication of pressure sensor, and SEM measurement, respectively. Z.L. synthesized the graphene. All authors discussed the results and contributed to the interpretation of data. Y.C. and P.S. cowrote the paper, with input from all coauthors. **Competing interests:** The authors declare that they have no competing interests. **Data and materials availability:** All data needed to evaluate the conclusions in the paper are present in the paper and/or the Supplementary Materials.

Submitted 11 April 2022
Accepted 28 July 2022
Published 14 September 2022
10.1126/sciadv.abq4824

ScienceAdvances

Nanofloating gate modulated synaptic organic light-emitting transistors for reconfigurable displays

Yusheng ChenHanlin WangFeng LuoVerónica Montes-GarcíaZhaoyang LiuPaolo Samorì

Sci. Adv., 8 (37), eabq4824.

Science Advances (ISSN) is published by the American Association for the Advancement of Science. 1200 New York Avenue NW, Washington, DC 20005. The title *Science Advances* is a registered trademark of AAAS.